Composites Part B 151 (2018) 222–231

Contents lists available at ScienceDirect

Composites Part B

journal homepage: www.elsevier.com/locate/compositesb

An atomistic study on the mechanical behavior of bamboo cell wall constituents

Huali Hao[a], Lik-ho Tam[b,1], Yang Lu[c,d], Denvid Lau[a,e,*]

[a] Department of Architecture and Civil Engineering, City University of Hong Kong, Hong Kong, China
[b] School of Transportation Science and Engineering, Beihang University, Beijing, 100191, China
[c] Department of Mechanical and Biomedical Engineering, City University of Hong Kong, Hong Kong, China
[d] Centre for Advanced Structural Materials, Shenzhen Research Institute of City University of Hong Kong, Shenzhen, 518057, China
[e] Department of Civil and Environmental Engineering, Massachusetts Institute of Technology, Cambridge, MA, 02139, USA

ARTICLE INFO

Keywords:
Bamboo constituents
Computational modeling
Mechanical properties
Microstructural evolution

ABSTRACT

Although the bamboo material has excellent mechanical properties, the anisotropic mechanical properties across and along the bamboo culm hinder its use as the structural material. As the bamboo fibers are the source of the mechanical properties for bamboo, a fundamental understanding on the structure and mechanical behaviors of bamboo fiber and its constituents enables us to figure out the origin of the anisotropic mechanical properties. In this work, the mechanical response of the cellulose, hemicellulose, and lignin under uniaxial tensile at the strain rate of $10^8\ s^{-1}$ is investigated by molecular dynamics simulation and the molecular conformational change under the tensile deformation is in situ captured. The breakage of the hydrogen bonds and slippage of the linear polymer chains are dominant for the failure of the cellulose. The normal stress dominated fracture mechanism is the key to the failure of the hemicellulose whereas the shear stress dominated fracture mechanism is the main failure mode for the lignin. The revealed relationship between the structure and mechanical properties of the cell wall constituents in bamboo fibers provides a guideline for assembling of the basic constituents and for modifying their structure to obtain a material that has isotropic mechanical properties and maintains the excellent mechanical properties of the bamboo.

1. Introduction

Bamboo with the advantages of sustainability, low cost, environmental friendliness, ready availability, low weight and commendable mechanical performance has received an increasing attention as a green construction material, a highly renewable biocomposite for industrial application, and a proficient template for bio-mimicking [1–3]. The bamboo as a typical fiber reinforced composite is mainly constituted by natural polymers: the major microstructural constituents (fibers and parenchyma cells) of bamboo are lamellar consisting of cellulose microfibrils embedded in the lignin and hemicellulose matrix, in which minor amounts (the weight fraction ranging from 5% to 10%) of extractives such as, waxes and gums are also present [4,5]. Numerous literature is focused on the mechanical properties of bamboo. For example, the flexural properties of bamboo in the axial direction, along with the compressive and tensile strengths in the axial and transverse directions have been measured [6,7]. Compared with other common building materials, bamboo is stronger than timbers, and its strength-to-weight ratio is greater than that of common wood, cast iron, aluminum alloy and structural steel [8,9]. As the bamboo is a kind of heterogeneous and anisotropic material, its mechanical properties vary significantly along and cross the culm [10]. Its density and mechanical properties increase both from the inner to outer part along the diametric direction and from lower to upper part along the longitudinal direction [11–14]. For example, the compressive strength of the moso bamboo varies from 40 MPa to 100 MPa along the axial direction and the axial flexural Young's modulus varies from 5 to 20 GPa along the diametric direction [2]. The anisotropy of mechanical properties hinders the bamboo used as a structural material. In order to explore the possibility of bamboo applied as a structural material, bamboo composites such as the bamboo scaffolding, laminated bamboo, and bamboo fiber reinforced composites have been fabricated and the mechanical properties of these bamboo composites have been measured [15–17]. However, all these investigations are mainly focused on the mechanical properties. The origin of the anisotropic

* Corresponding author.Department of Architecture and Civil Engineering, City University of Hong Kong, Hong Kong, China.
E-mail address: denvid@mit.edu (D. Lau).
[1] Co-first author.

https://doi.org/10.1016/j.compositesb.2018.05.046
Received 6 January 2018; Received in revised form 13 May 2018; Accepted 27 May 2018
Available online 28 May 2018
1359-8368/

mechanical properties across and along the culm are not well understood. As the bamboo fibers made up of cell walls are the source of the mechanical properties for bamboo, a fundamental understanding on the structure and mechanical behaviors of bamboo fiber and its constituents can enable us to figure out the macroscopic behavior of bamboo. Meanwhile, the revealed relationship between the structure and mechanical properties of the cell wall constituents in bamboo fibers provides a guideline for assembling of the basic constituents to design the new structural material with excellent and homogeneous properties.

Molecular dynamics (MD) simulations can depict the microstructure evolution, such as the rearrangement of atoms, the change of polymer chain conformation, the intermolecular interaction and the intramolecular interaction [18–23]. MD simulations have become a powerful approach to explore the dynamical processes of configuration changes and to predict mechanical properties, quantifying their relationship to the microstructure [24–26]. The obtained chemical structure information of bamboo from experiments permits the atomistic modeling of the molecular structure by using MD simulations [27–31]. Efforts have been paid to the chemical composition and molecular structure of cellulose, hemicellulose and lignin. MD simulations have been successfully applied to build a bottom-up model starting from the chemical structure of basic constituents in bamboo and to predict the mechanical behavior of the constitutive molecules out of current capability of experiments. For example, the structure of cellulose microfibrils embedded in a matrix of amorphous hemicellulose and lignin has been built to predict the mechanical properties [32,33]. It is found that the adhesion energy between the matrix and the cellulose determines the bond strength of cell wall materials and the amorphous structures in cell wall have key roles in the variation of elastic modulus with increasing the moisture content. There is a fundamental limitation of conventional MD simulations that they can only handle the timescale of less than microseconds far from the realistic timescale [34]. The conventional MD prevents an accurate understanding of microstructure evolution during deformation. The autonomous basin climbing algorithm can be applied to extend the timescale of atomistic simulations beyond the reach of MD simulations. The simulation starts at the modeled structure equilibrated with the minimized potential energy and the modeled structure moves to the next state where the system is of local minimized potential energy by applying an extensional condition [35–37]. The exploration of the system moved to one state with local minimized energy can ensure the occurrence of the plasticity of the modeled structure, giving reasonable qualitative results for the deformation behavior of modeled structures.

The objective of this study is to investigate the mechanical behavior of bamboo cell wall constituents, namely cellulose, hemicellulose, and lignin, so as to understand the origin of the anisotropic mechanical properties across and along the culm. The scope of this work is to firstly model the structures of bamboo constituents by using atomistic modeling approach. The modeled structures in equilibration are subjected to the tensile deformation at a fixed strain rate of $10^8\ s^{-1}$ to analyze their mechanical response. Through the in-situ capture of the molecular conformations associated with the evolution of modeled structures under the tensile deformation, the relationship between the microstructures and mechanical properties of the cell wall constituents in the bamboo fiber can be disclosed. By comparing the mechanical behavior of different cell wall constituents, it provides an insight into the anisotropy and inhomogeneity of bamboo properties across and along the culm. Furthermore, the bamboo has excellent properties to overcome the confliction between the toughness and the strength inspiring one to design and to fabricate bio-inspired structural materials [38–40]. For example, the bamboo fibers are composed of several layered cell walls and each cell wall is made up of cellulose microfibrils embedded in the amorphous matrix, which inspires us to design the crystal microfibrils reinforced polymer composites with enhanced mechanical properties compared to the pure polymer.

2. Simulation details

2.1. Molecular modeling

In this work, the initial microstructures of cellulose, hemicellulose and lignin are generated in the Materials Studio software from Accelrys [41]. The cellulose fibril has a crystalline structure revealed by experiments [27]. The crystalline cellulose I_β has been found to be predominant in the bamboo and accordingly is chosen as the representative cellulose model [4]. The cellulose has a monoclinic unit cell with dimensions of a = 7.8 Å, b = 8.2 Å, c = 10.4 Å and an angle $\gamma = 96.5^\circ$ at the *ab* plane. There are two parallel chains in the unit cell where one chain (the origin chain) is positioned at the corner of the unit cell parallel to the *c* axis direction, and the second chain (the center chain) passes through the center of the *ab* plane. Each chain in the unit cell is made up of two glucose residues linked by the β (1–4) glycosidic linkage [42,43]. Linear cellulose chains where glucose rings are covalently connected are held together by inter-chain hydrogen bonds to form cellulose layers. The hemicellulose of the xylene type is used as a representative for hemicellulose structure. The hemicellulose structure includes two types of segments: one segment of 5 D-xylopyranosyl residues covalently connected and another segment with an L-Arabinofuranosyl residue linked to the third xylosyl residues by an α-(1–3) linkage. The weight ratio between two segments is about 1. The segments are added in sequence with random orientation and an equilibration is performed after every adding step. Specifically, one segment of 5 D-xylopyranosyl residues is added, which is followed by equilibration in the isothermal and isochoric (NVT) ensemble at 298 K and in the isothermal and isobaric (NPT) ensemble at 298 K and 1 atm. After that, one segment consisting of 5 D-xylopyranosyl residues and 1 L-Arabinofuranosyl residue is added, which is followed by the equilibration as described previously. The addition of two types of the segments is repeated, and the final hemicellulose molecule has a length of 10 nm and a thickness of 4 nm as close to the cellulose model. Lignin molecules have various composing units and different linkages between the units. The lignin includes three basic structural sub-units namely *p*-hydroxyphenyl, guaiacyl and syringyl units and the proportions of these basic structures vary greatly in different bamboos. The percentage and sequence of interunit linkages are also different in different bamboos. In order to reduce the complexity, the amorphous lignin molecule is formed by the polymerization of the most common syringyl unit with the linkage of β-O-4 in the bamboo [4]. Because the volume fraction of three units for the lignin in the bamboo is the 67–78% of syringyl, 21–31% of guaiacyl and 1–2% of *p*-hydroxyphenyl and the predominant intermonomer linkage is of the type β-O-4 (45–49% per 100 monomers) through the experimental measure [44]. The simplified modeled structure of lignin where syringyl units are linked through β-O-4 linkage has been used to predict its viscoelasticity and the simulated results have a good agreement with the experimental results [7]. The units and modeled structure for cellulose, hemicellulose and lignin are shown in Fig. 1. After the initial microstructure is generated, the geometry optimization and energy minimization by conjugate gradient method are performed at room temperature (298 K) to ensure the equilibration and stability of the modeled structures. Each model is equilibrated for 1 ns in the NVT ensemble at 298 K, followed by another 1 ns equilibrated in the NPT ensemble at 298 K and 1 atm. The densities of modeled structures for cellulose, hemicellulose and lignin shown in Table 1 are 1.56 g/cm^3, 1.49 g/cm^3 and 1.35 g/cm^3 respectively. They are close to the experimental measurement [7, 32 45]. The glass transition temperature of the modeled hemicellulose and lignin are also shown in Table 1. The glass transition temperatures for the hemicellulose

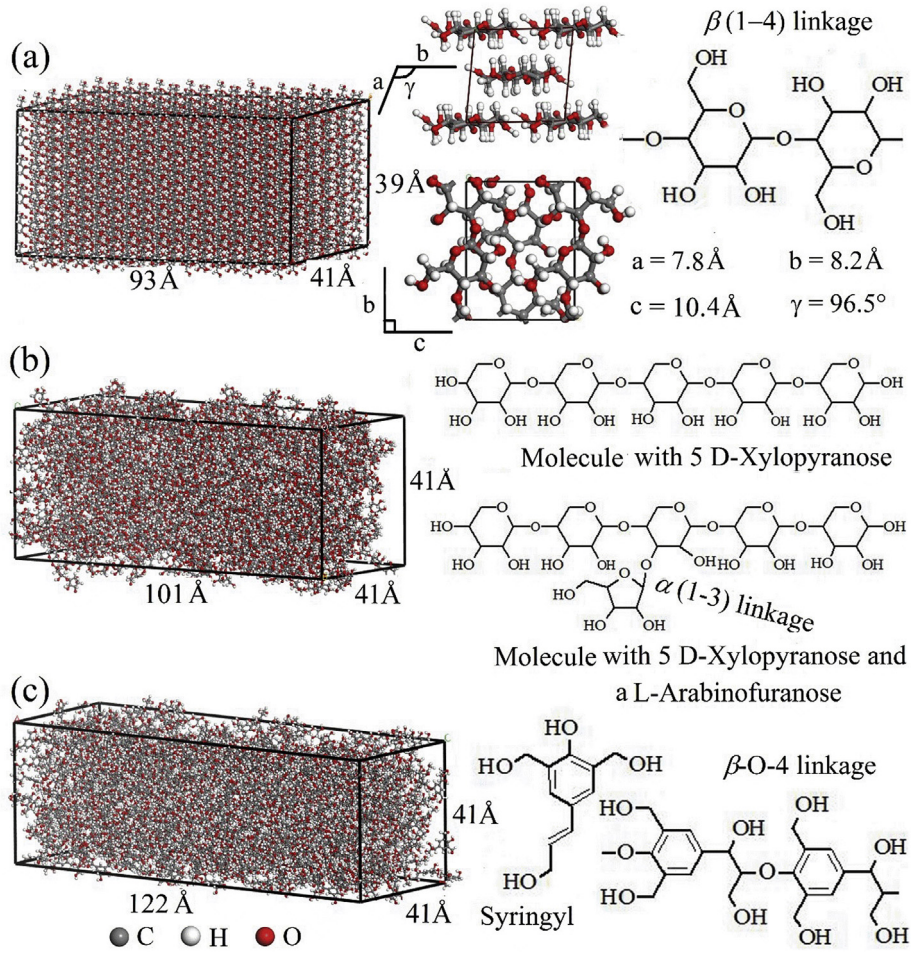

Fig. 1. (a) The modeled crystal structure of the cellulose. The crystal cellulose is of the monoclinic structure. The linear chain structure is made up of glucose molecules which are linked by the β (1–4) glycosidic linkage. The adjacent chains are linked by hydrogen bonding. (b) The modeled amorphous structure of the hemicellulose. It consists of two kinds of molecules: the molecular formula of 5 D-Xylopyranose and the molecular formula of 5D residues with an L-Arabinofuranose linked to the third xylosyl residues of 5D by an α-(1–3) linkage. (c) The modeled amorphous structure of the lignin. It is made up of β-O-4 linked syringyl units.

and lignin are 46 °C and 89 °C respectively. The simulated results are very close to the experimental data where the glass transition temperature of the hemicellulose is about 40 °C and that temperature of the lignin is 50 °C–100 °C [46].

The selection of a forcefield is an important step in atomistic simulations because it determines the accuracy in predicting properties related to atom interactions of materials [47–49]. The potential energy comprises a set of covalent related interactions such as the bond interaction between pairs of bonded atoms, the angle interaction between three consecutive bonded atoms, the dihedral and the improper interaction between quadruplets of atoms and non-bonded interactions like van der Waals interaction and the Coulombic interaction. These interactions dominate the mechanical deformation of molecular materials. Specifically, the covalent related potential energy depends on the bond lengths, bond angles, torsion angles and improper out-of-plane angles. The non-boned potential energy is determined by the Van der Waals interactions and Coulomb interactions. The condensed-phased optimized molecular potential for atomistic simulation studies (COMPASS) is chosen as it can predict the structural, conformational and vibrational properties of a broad range of molecules in condensed phases and has an experimentally comparable precision in predicting molecular properties in condensed phases [50].

The COMPASS potential function is expressed as [51]:

Table 1
Predicted Young's modulus *E*, density (ρ) and glass transition temperature (T_g) by the COMPASS forcefiled for different constituents, compared with the experimental results.

	E (GPa)		ρ (g/cm^3)		T_g (°C)	
	Experiment	MD	Experiment	MD	Experiment	MD
Cellulose	120-140 [7]	142	1.45–1.59 [7]	1.56	-	-
Hemicellulose	3.50–8.00 [32]	5.90	1.46–1.79 [45]	1.49	40 [46]	46
Lignin	2.00–6.70 [32]	5.45	1.33–1.38 [45]	1.35	50-100 [46]	89

$$
\begin{aligned}
U=&E_b + E_\theta + E_\phi + E_\chi + E_{b,b1} + E_{b,\theta} + E_{b,\phi} + E_{\theta,\theta1} + E_{\theta,\phi} + E_{\theta,\theta1,\phi} \\
&+ E_{Coul} + E_{LJ} \\
E_b =& \sum_b [K_2(b-b_0)^2 + K_3(b-b_0)^3 + K_4(b-b_0)^4] \\
E_\theta =& \sum_\theta K_2(\theta-\theta_0)^2 + K_3(\theta-\theta_0)^3 + K_4(\theta-\theta_0)^4] \\
E_\phi =& \sum_\phi [K_1(1-\cos\phi) + K_2(1-\cos 2\phi) + K_3(1-\cos 3\phi)] \\
E_\chi =& \sum_\chi K\chi^2 \\
E_{b,b1} =& \sum_{b,b1} K(b-b_0)(b-b_1) \\
E_{b,\theta} =& \sum_{b,\theta} K(b-b_0)(b-\theta_0) \\
E_{b,\phi} =& \sum_{b,\phi} (b-b_0)(K_1\cos\phi + K_2\cos 2\phi + K_3\cos 3\phi) \\
E_{\theta,\theta1} =& \sum_{\theta,\theta1} K(\theta-\theta_0)(\theta-\theta_1) \\
E_{\theta,\phi} =& \sum_{\theta,\phi} (\theta-\theta_0)(K_1\cos\phi + K_2\cos 2\phi + K_3\cos 3\phi) \\
E_{\theta,\theta1,\phi} =& \sum_{\theta,\theta1,\phi} K(\theta-\theta_0)(\theta-\theta_1)\cos\phi \\
E_{Coul} =& \sum_{i,j} \frac{q_i q_j}{4\pi D r_{ij}} \\
E_{LJ} =& \sum_{i,j} \varepsilon_{ij}\left[2\left(\frac{R_{min,ij}}{r_{ij}}\right)^9 - 3\left(\frac{R_{min,ij}}{r_{ij}}\right)^6\right]
\end{aligned}
\tag{1}
$$

The functions can be divided into two categories: valence terms including diagonal and off-diagonal cross-coupling terms and non-bond interaction terms. The diagonal valence terms include the bond term (E_b) related to the bond length (b), the angle term (E_θ) correlated to the bond angle (θ), the dihedral angle torsion term (E_ϕ) related to dihedral angle (ϕ) and the improper angle term (E_χ) correlated to the improper angle (χ). The cross-coupling terms include combinations of two or three internal coordinates, namely the bond-bond term ($E_{b,b1}$), the bond-angle term ($E_{b,\theta}$), the bond-torsion term ($E_{b,\phi}$), the angle-angle term ($E_{\theta,\theta1}$), the angle-torsion term ($E_{\theta,\phi}$) the angle-angle-torsion term ($E_{\theta,\theta1,\phi}$). The b_0 and b_1 represent the equilibrium bond length. The θ_0 and θ_1 represent the equilibrium bond angle; the b, θ, ϕ and χ are bond length, bond angle, dihedral angle and improper angle respectively. The non-bond interactions include a 9-6 Lennard-Jones potential function for the van der Waals term and a Coulombic function for an electrostatic interaction and are used for interactions between pairs of atoms that are separated by two or more intervening atoms or those that belong to different molecules. In the simulation, the van der Waals and Coulombic interactions are truncated at a cutoff distance of 10 Å in the simulation. As the Coulombic interaction is taken into consideration, it is important to accurately predict the charge distribution of the atoms. The charge equilibration approach can predict the charge distribution in agreement with experimental dipole moments and other simulation results of protein and carbohydrates [50]. The Coulombic interaction as a part of the non-bonded interaction directly affects the potential energy calculation of the system. The mechanical properties of different constituents are predicted by using MD simulations with COMPASS force field. The MD simulations are carried out using the parallel MD code LAMMPS [52]. The results of Young's modulus are represented in Table 1, compared with the experimental data. The E of the cellulose, hemicellulose and lignin are 142 GPa, 5.90 GPa and 5.45 GPa respectively. The simulated Young's modulus is located in the range of experimental results indicating the reliability of the COMPASS forcefiled to predict the mechanical properties of the bamboo constituents.

2.2. Simulation methods

The autonomous basin climbing algorithm is an adaptation of metadynamics approach to enhance the sampling. In the metadynamics approach, the penalty potential acts on a selected number of degrees of freedom in the system by adding to the system Hamiltonian, and the driving force is derived from the Gibbs potential. However, the penalty potential acts on all the atomistic degrees of the freedom in the modeled system in autonomous basin climbing algorithm. The system is driven from its current configuration to the next equilibrated configuration by imposing a prescribed energy penalty function to the potential energy. The autonomous basin climbing method can provide details of the molecular conformation giving an insight into mechanisms of activation and relaxation, and also allow an interpretation of phenomena related to the interatomic interactions by tracking system evolution. Firstly, an initial structure with minimized potential energy is activated by adding a penalty function. Subsequently, after the energy minimization, the structure with a minimized potential energy overcoming the energy barrier moves to another state with a local minimum energy. In our simulation, a Gaussian function is chosen as the penalty function expressed by Ref. [34]:

$$\Phi_i(\boldsymbol{r}) = \omega \exp[-(\boldsymbol{r} - \boldsymbol{r}^i_{\mathbf{min}})^2/2\sigma^2] \tag{2}$$

where $\boldsymbol{r}^i_{\mathbf{min}}$ is the minimum energy configuration, the ω and σ determine the strength and width of the penalty function. The added penalty function drives the system from its initial configuration into a higher energy state. Generally, a large width and strength accelerate the energy increment per timestep and allow the atoms to escape from the initial state with the minimized potential energy in fewer steps. The large increment in energy per timestep can result in the missing of some molecular conformation associated with the evolution of the modeled system, which can reduce the accuracy of the simulation. Meanwhile, the decrease of the width and strength reduce the energy increment per timestep, which requires more simulation timesteps to the state where the crack of the simulated samples occurs. Taken all these into consideration, the chosen ω is 0.1kal/mol and the σ is 0.1 Å ensuring the reasonable computational cost of simulations. If the system cannot overcome the energy barrier, it returns to the initial state with minimized potential energy. Otherwise, the system reaches to another state where the local minimum energy is higher than the global minimum energy of the initial state. The energy barrier ΔE between the initial state and the state that the system is of the highest energy is calculated. The activation time is defined by Ref. [53]:

$$\Delta t = [10^{13}\exp(-\Delta E/k_B T)^{-1}] \tag{3}$$

where k_B is the Boltzmann constant and T is the temperature. A fixed strain rate ($\bar{\varepsilon}$) of $10^8\ s^{-1}$ is imposed for deformation. The corresponding strain increment during Δt is calculated by $\Delta\varepsilon = \bar{\varepsilon}\Delta t$. We theoretically derive the impact of applied strain rate on the activated interaction processes by assuming that the initially minimized configuration $\boldsymbol{r}^i_{\mathbf{min}}$ ($\boldsymbol{r}$ means the atom coordinates of the system.) moves to the next minimum configuration $\boldsymbol{r}^{i+1}_{\mathbf{min}}$ as the result of the strain increment of $\Delta\varepsilon_i$. The $\Delta\varepsilon_i$ is applied to the initial system to get a new configuration $\boldsymbol{r}^{i+1}_{\mathbf{min},1}$. The sampling process is repeated to get the transition time to the next nearest minimum configuration and the corresponding strain increment $\Delta\varepsilon$ at the strain rate of $10^8\ s^{-1}$ can be obtained according to equation (3). The strain increment is applied along the z direction to model the uniaxial tensile deformation. The configuration $\boldsymbol{r}^{i+1}_{\mathbf{min},1}$ is moved to a new state by applying the strain increment of $\Delta\varepsilon_{i+1}$. By repeating the sampling process to get the transition time and corresponding strain increment following by the strain increment is imposed to the system along the z direction, the tensile deformation at a fixed strain rate can be modeled. The corresponding molecular conformational change can be captured.

3. Results and discussion

The radial distribution functions (RDF) are calculated to quantify the bond types and length in the modeled hemicellulose and lignin. RDF is the probability density of finding atoms A and B at a distance r averaged over the equilibrium trajectory. Fig. 2 shows the RDF of C-C, C-O, C-H and O-H atoms in the hemicellulose and lignin. The first highest peak of the C-C curve in Fig. 2(a) is about 1.55 Å, while this of C-C curve in Fig. 2(b) is about 1.45 Å. It is because the bond type of C-C in the hemicellulose is sp^3-sp^3 with the C-C bond length of 1.55 Å [54].

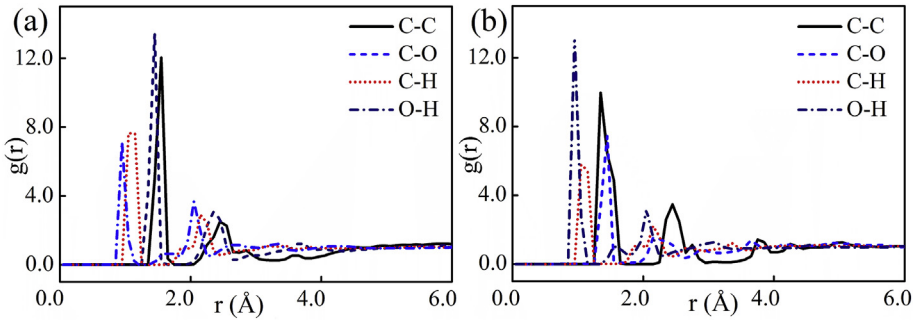

Fig. 2. Radial distribution functions of C-C, C-O, C-H and O-H atoms in (a) hemicellulose and (b) lignin. The first highest peak of the C-C curve in (a) is about 1.55 Å, while this of C-C curve in (b) is about 1.45 Å. The bond length of the C-O, C-H, and O-H in the hemicellulose and lignin are similar, which are 1.45 Å, 1.05 Å and 0.95 Å respectively. The second highest peak of the O-H curve in the hemicellulose and lignin is about 2.05 Å. It represents the length of hydrogen bonds. The higher of this peak for the hemicellulose indicates more hydrogen bonds are formed in the hemicellulose.

However, there are two types of C-C bond in the lignin (namely sp^3-sp^3 type and C-C type in benzene). The C-C bond length in benzene is 1.39 Å [55]. The bond length of the C-O, C-H, and O-H in the hemicellulose and lignin are similar, which are 1.45 Å, 1.05 Å and 0.95 Å respectively. These results are close to the experimentally measured data, which are 1.43 Å, 1.1 Å, and 0.96 Å for the C-O, C-H, and O-H bonds respectively [54,56,57]. The second highest peak of O-H in the hemicellulose and lignin is about 2.05 Å, representing the length of a hydrogen bond. The higher of this peak for the hemicellulose indicates more hydrogen bonds are formed in the hemicellulose.

The modeled cellulose, hemicellulose and lignin show different mechanical behaviors as shown in Fig. 3. The cellulose is subjected to progressively increasing stress to reach the maximum stress and then the stress drops rapidly until the failure occurs. There is a decrease in the increment rate of the stress when the strain is larger than around 0.082 as the point A in Fig. 3(a). The stress-strain curves of the hemicellulose and lignin follow the typical trend with an elastic regime at the beginning stage of the deformation shown in Fig. 3(b) and (c). The stress gradually increases with a non-linear relationship to the strain as the tensile deformation continues. They display different stress-strain response at the descending branch of the diagram. There is a slight reduction in stress for the hemicellulose before the stress rapidly drops with increasing the strain as shown in Fig. 3(b). However, the stress of the lignin reduces with increasing the strain. By comparison, it is found that the strength of the cellulose is significantly higher than that of the hemicellulose and lignin. The cellulose fails with a sudden drop of stress whereas the hemicellulose and lignin are broken with a relatively gradual decrease of stress. It indicates the cellulose mainly provides the strength of the bamboo and the matrix of hemicellulose and lignin is benefited to load transform between cellulose microfibrils. Our simulated results are consistent with both experimental data [7] and simulated results [5]. For example, the experimental results have shown the strength of the cellulose is up to 1 GPa and the strength of the hemicellulose and lignin is around 50 MPa [7]. The role of the cellulose is mainly to resist the mechanical loading and the role of the hemicellulose and lignin is mainly to enhance the elongation studied by the atomistic simulations [5].

The microstructural evolution is characterized to explain the difference of stress-strain response. Fig. 4(a) shows the failed structure of the modeled cellulose and the details of the structure at the region *a* in Fig. 4(a) projected at the (100) plane at different strains are represented in Fig. 4(b)–(f). Here, it is defined that the torsion angles φ and ψ denote the rotation around C1-O1 and C4-O1 bonds respectively. It is obvious that the valent angle (θ) of glycosidic bonds (C1-O1 and C4-O1) increases from initial 115° (Fig. 4b) to nearly 180° when the modeled cellulose fails (Fig. 4e). The increment of valent angels is related to the effect of the rotation of φ and ψ. The magnified molecular structures of glucose molecules in Fig. 4(b) and (e) are shown in Fig. 4(c) and (f) respectively. Compared with the molecular structure in Fig. 4(c), the glycosidic bonds are stretched, and the glucose rings are almost in a similar plane in Fig. 4(f). These are the reasons for the polymer chains are highly linearized when the modeled cellulose fails. The corresponding structures projected at the (001) plane are shown in Fig. 4(g)–(i). The polymer chains at the (100) plane are almost parallel to the polymer chains at the (200) plane in Fig. 4(g). The displacement *d* between the (200) and (100) planes is equal to *c*/4 where *c* is the

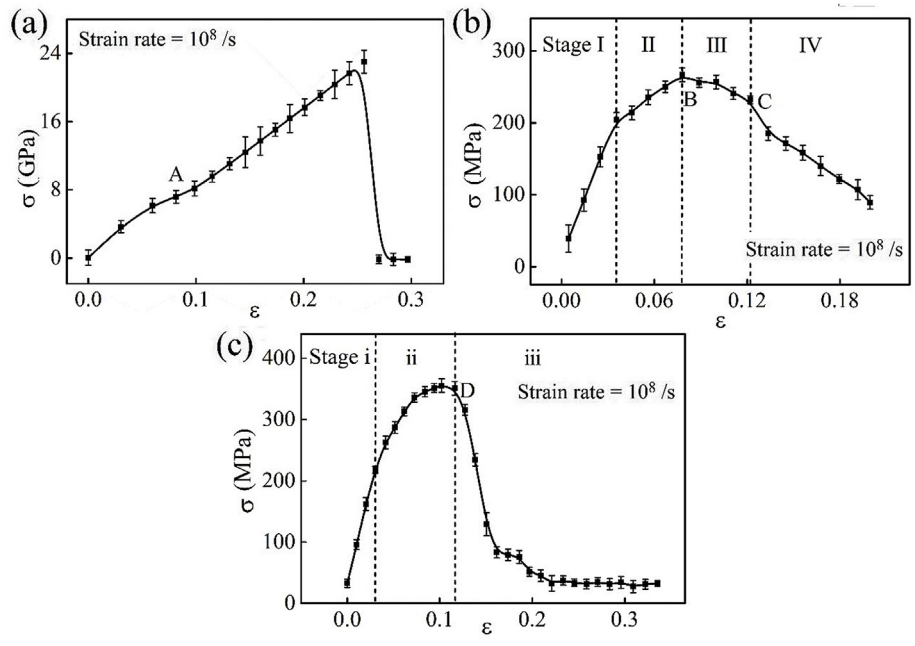

Fig. 3. The stress-strain curves of different constituents: (a) cellulose; (b) hemicellulose; (c) lignin. The modeled structures of the cellulose and hemicellulose and lignin keep an elastic deformation at the beginning of the deformation. The stress-strain is non-linear with the increment of the strain. The different response of stress to strain between the hemicellulose and the lignin is because that the hemicellulose is made up of short branched polymer chains whereas the lignin consists of cross-linked polymer chains.

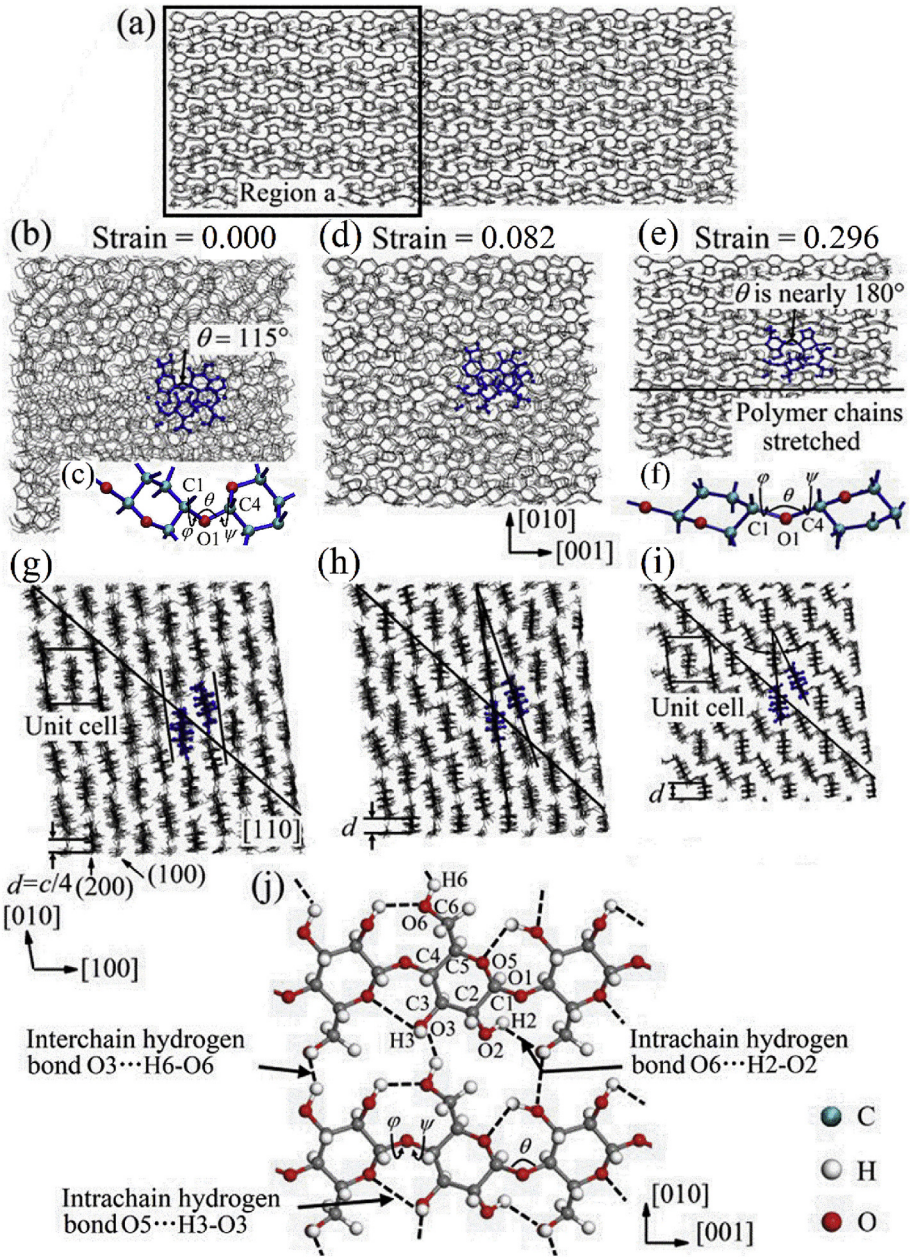

Fig. 4. The snapshots of structural evolution for the cellulose at different strains. The region with blue color in different figures represents the molecular conformation of the same glucose molecules. (a) The failed structure of the modeled cellulose. (b) The initial structure of the region *a* projected at the (100) plane. (c) The magnified structure of glucose molecules in (b) where θ is the valence angle; φ and ψ are torsion angles denoting the rotation around C1-O1and C4-O1 bonds respectively. (d) and (e) The structure of the region *a* projected at the (001) plane at the strain of 0.082 and 0.296 respectively. The polymer chains are stretched and become linear with the increment of θ in (e). (f) The magnified structure of glucose molecules in (e). (g) The initial structure of the region *a* projected at the (001) plane. (h) and (i) The structure of the region *a* projected at the (001) plane at the strain of 0.083 and 0.296 respectively. The angle between the polymer chains at (100) plane and those at the (200) plane caused by the polymer rotated is increased in (i). The displacement *d* between (200) and (100) planes has an obvious increment indicating the slippage of polymer chains in (i). (j) The hydrogen bonds formed in the initial cellulose structure. (For interpretation of the references to color in this figure legend, the reader is referred to the Web version of this article.)

distance of unit cell in [001] direction. The polymer chains are rotated along < 110 > direction when the strain is increased to 0.082 in Fig. 4(h). The rotation of polymer chains results in an angle between the polymer chains at the (100) plane and those at the (200) plane as the black lines shown in Fig. 4(h). The *d* has a little increment indicating the slippage of polymer chains. The angle between the polymer chains at the (100) plane and those at the (200) plane is significantly increased associated with the increment of *d* when the cellulose fails in Fig. 4(i). The rotation and slippage of polymer chains at different {100} planes are correlated to the non-bonded interaction between polymer chains. Hydrogen bonds are formed between polymer chains at {100} planes while the polymer chains at the (100) plane interact with the nearest neighbor chain at the (200) plane by the van der Waals force [58]. The van der Waals force is increased during the tensile deformation leading to the rotation of polymer chains along the < 110 > direction [59]. Fig. 4(j) shows the hydrogen bonds in the initial structure of cellulose. The intrachain hydrogen bonds are dominated by the O5···H3-O3 and O6···H2-O2 and the interchain hydrogen bond is dominated by the O3···H6-O6 at the (100) plane [58,59]. The initial number of hydrogen bonds in modeled cellulose is about 1142. Due to the stretch of the polymer chains and the bending of valent angles during the tensile deformation, the distance of the atoms to form the hydrogen bonds is increased and larger than the detected distance indicating the breakage of the hydrogen bonds. The number is reduced to nearly zero after the failure of the cellulose. The presence of a hydrogen bond is detected by a minimum oxygen-hydrogen-oxygen angle of 100° and a cutoff distance of 3.5 Å.

Although both the hemicellulose and lignin are amorphous, the hemicellulose is made up of two segments with short branched polymer chains while the lignin is formed by the polymerization of syringyl units with crosslinked polymer chains. The different configuration of polymer chains is the primary reason for their different stress-strain response. Figs. 5 and 6 show the microstructural evolution of the hemicellulose and the lignin during the deformation. Specifically, Fig. 5(a) shows the cracked structure of the modeled hemicellulose and Fig. 5(b)–(e) show the conformational change of the region *b* in Fig. 5(a) at different strains. Compared with the initial structure at the region *b* in Fig. 5(b), the cross-section of the modeled structure at the

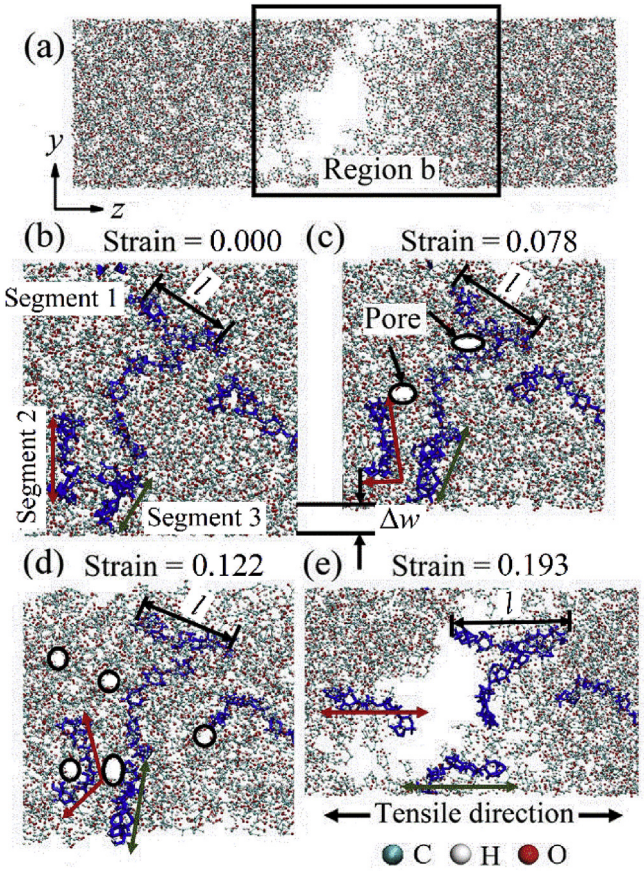

Fig. 5. The snapshots of structural evolution for the hemicellulose at the different strains. The bonds with blue color show the evolution of the same atoms during the tensile deformation. (a) The final failed structure of the modeled hemicellulose. (b) The corresponding initial structure of the region *b* in (a). The segments of molecules are randomly distributed. (c) The corresponding structure of the region *b* at the strain of 0.078. There are pores generated. The polymer chains are stretched with the increase of the chain length and rotated. The cross-section is reduced. (d) The corresponding structure of the region *b* at the strain of 0.122. The number of pores rises. (e) The magnification figure of the failed structure of the region *b*. The chains are almost distributed along the tensile direction. (For interpretation of the references to color in this figure legend, the reader is referred to the Web version of this article.)

strain of 0.078 is reduced about Δw as shown in Fig. 5(c). The length of segments is increased and the polymer chains are rotated. Moreover, pores are observed. When the strain is risen to about 0.122, the cross-section has a little change due to the increment of pores in Fig. 5(d). An obvious reduction of the cross-section is observed when the modeled hemicellulose cracks shown in Fig. 5(e). The stretched polymer chains near the break region are approximately parallel to the tensile direction. Fig. 6(a) shows the cracked structure of the modeled lignin and the conformational change of the region *c* in Fig. 6(a) at different strains are represented in Fig. 6(b)–(d). The polymer chains are rotated associated with the obvious shrinkage of the cross-section and pores are generated at the strain of 0.116 as shown in Fig. 6(c). The polymer chains are distributed along a direction of an angle with respect to the tensile direction when the modeled lignin is cracked as shown in Fig. 6(d). By tracking the conformational change of the same molecules at different strains, the molecular segments are stretched. It can be found the tensile stress dominates the failure of the hemicellulose, whereas the shear stress plays a critical role in the failure of the lignin.

Fig. 7 shows the corresponding potential energy and the energy of valence interaction change with increasing the strain of the hemicellulose and lignin. The increase of the potential energy change at the elastic stage (stage I and i) for the hemicellulose and lignin is mainly correlated to the increment of non-bonded energy as shown in Fig. 7(a) and (c) respectively. The valence interactions make a contribution to the change of potential energy in the progressive deformation. The change of the covalent related energies is caused by different reasons for the hemicellulose and lignin. Specifically, there is a negligible change in the bond related energy (E_{bond}) and improper angle related energy (E_{imp}) for the hemicellulose during the deformation as shown in Fig. 7(b). The chang of the bond angle related energy (E_{angle}) for the hemicellulose decreases at the non-linear stage (stage II), and then increases until the crack occurs (stage III and IV). The change of the dihedral angle related energy (E_{dihed}) gradually decreases with the increment of the strain as the gauche conformations rotate to the trans conformations with a lower energy [60,61]. It indicates the mobility of polymer chains in the modeled hemicellulose is dependent on the angle bending and the dihedral rotation. All these result in the potential energy change increasing until to the stage III and finally reducing at stage IV. Consequently, the deformation of the modeled hemicellulose is dominant by the non-bonded interaction at the elastic stage followed by the covalent related energy dominated. The change of the angle bond related energy of the lignin also decreases at the non-linear region (stage ii) and then increase at stage iii. The change of the dihedral angle related energy steadily decreases associated with the chains rotation. The energies correlated to the bond length and improper dihedral angle do not change significantly. As a result, the majority of deformation in the polymer system is accommodated via angle bending, dihedral rotations, and non-bonded interactions. As the crosslinked polymer chains have stronger attraction forces than shorter branched polymer, more energy is required for the crack of the lignin leading to it has a higher

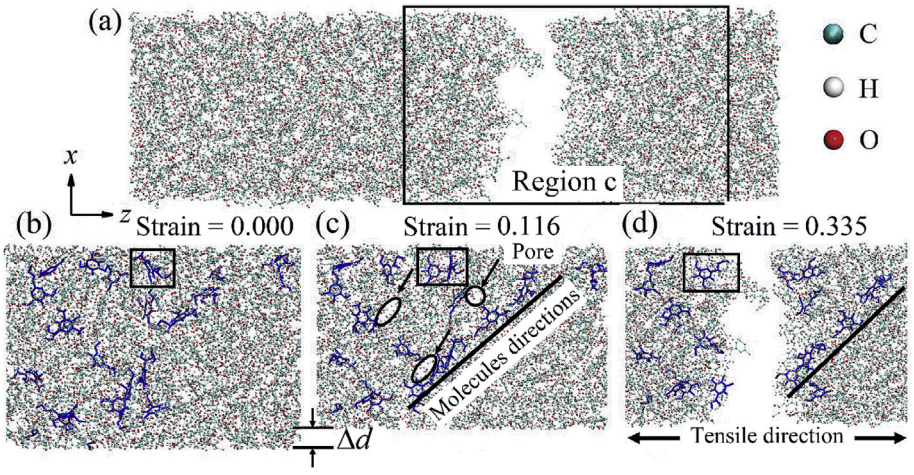

Fig. 6. The snapshots of structure for the lignin at the different strains. The bonds with blue color show the deformation of the same benzene rings before and after the rupture. (a) The failed structure of the lignin. (b) The initial structure of the region *c* where the basic syringyl units are randomly distributed in the initial structure. (c) The structure of the region *c* at the strain of 0.116. The molecules are tilted towards a similar direction. The direction of molecules distributed has an angle with respect to the tensile direction. There are pores formed. The cross-section significantly shrinks with Δd compared with the initial structure. (d) The magnification figure of the failed structure for the region *c*. Through the tracking the motion for the same molecule labeled with a rectangle in (b), (c) and (d), the polymer chains are stretched. (For interpretation of the references to color in this figure legend, the reader is referred to the Web version of this article.)

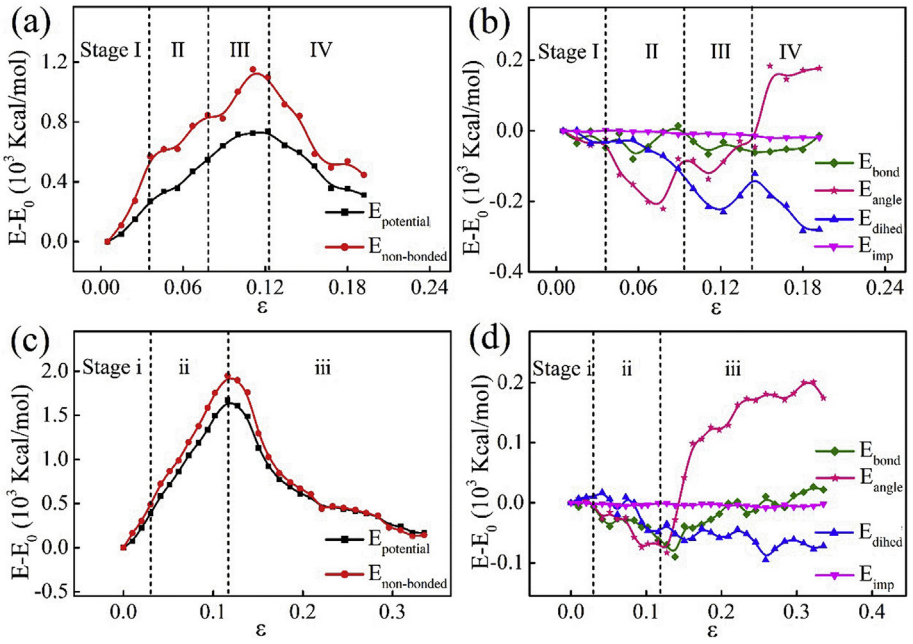

Fig. 7. The energy change during the tensile deformation for different modeled amorphous structures. (a) The potential energy and the non-bonded energy change for the hemicellulose. (b) The change of the bond related energy, bond angle related energy, dihedral angle related energy and improper angle related energy for the hemicellulose. (c) The potential energy and the non-bonded energy change for the lignin. (d) The change of the bond related energy, bond angle related energy, dihedral angle related energy and improper angle related energy for the lignin. The potential energy change at the elastic stage is caused by the non-bonded interactions. The covalent related energy plays a significant role in the progressive deformation. The bond related energy and improper angle related energy almost keep constant during the deformation. The change of the angle related energy decreases and then increases. The change of the dihedral angle related energy continuously decreases. It indicates the main molecular confirmation change during deformation involves the bending and rotation of the chains.

maximum stress.

The scheme to indicate the molecular conformation evolution of modeled crystal polymer structure and amorphous structure during the tensile deformation at the strain rate of $10^8\ s^{-1}$ is shown in Fig. 8. Fig. 8(a) shows the conformational change in a domain of one layer where the hydrogen bonds are formed between polymer chains before and after the modeled crystal structure fails. The valence angle and the length between two molecules are increased with the increment of strain leading to the stretch of the polymer chains. With the increment of the strain, the distance between the donor and acceptor atoms to form hydrogen bonds is increased resulting in the breakage of hydrogen bonds. The polymer chains at one layer interact with the polymer chains at the nearest neighbor layers through the van der Waals force. The van der Waals force is increased during the tensile deformation causing the rotation and slippage of polymer chains. Due to the limitation of the force field, the dissociation of the covalent bonds in the polymer chains does not take into consideration in this work. Through the experiment on stretching individual carboxyamylose polymers, it is found that the covalent bonds break when the displacement of the polymer chain is long, resulting in that in the long-range, van der Waals and electrostatic forces no longer act within molecules [62]. The deformation of the crystal polymer involves the alignment of the polymer chains, the slippage of lamellar planes and the breakage of the covalent bonds [63]. Although the polymer chains of the hemicellulose are branched and the polymer chains of the lignin are crosslinked, the conformational changes for both modeled hemicellulose and lignin under the tensile deformation are similar. The chains are stretched and then aligned towards the aligned direction. These crystallized structures can restrict the flow of one chain to another [64,65]. Fig. 8(b) shows the conformational change of crosslinked amorphous structure of the lignin. The chemical crosslinks prevent large polymer chain motion resulting in a stress-strain curve with a high strength [66].

Our work demonstrates the molecular conformational evolution of the cell wall constituents in the bamboo fiber during the tensile deformation at the strain rate of $10^8\ s^{-1}$. In reality, the anisotropic mechanical properties of the bamboo are correlated to the inconsistent

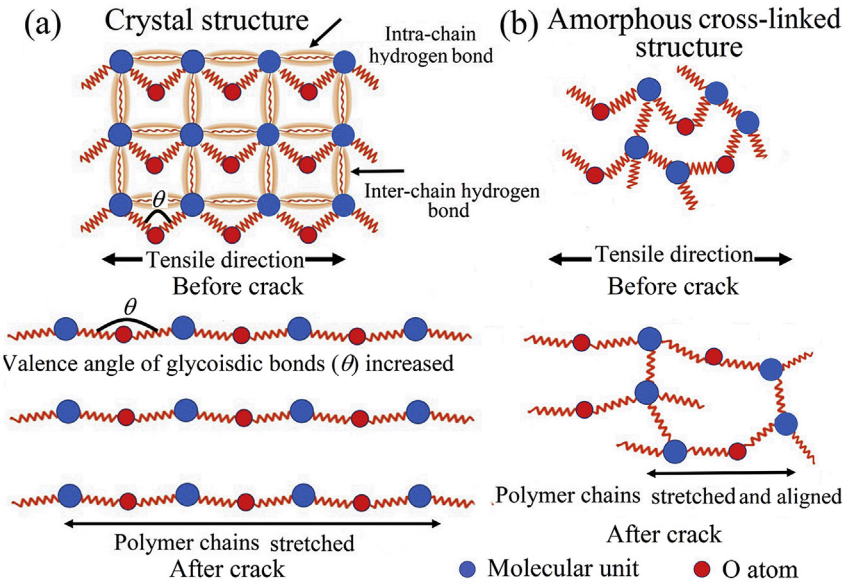

Fig. 8. Illustration of conformational change under the tensile deformation with the strain rate of $10^8\ s^{-1}$ for (a) the crystal structure of the cellulose and (b) the crosslinked amorphous structure of the lignin. The boundary condition of the structure is the periodic boundary condition. Note: Due to the limitation of the forcefield, the breakage of covalent bonds is not able to be simulated. In our work, the breakage of covalent bonds does not take into consideration. The ignorance may cause an effect on the value of the strength, while it does not affect both the stress change with the increment of the strain and the major microstructural evolution during tensile deformation. As we consider more about the relationship between molecular conformational evolution and mechanical response, the results and analysis of our work are still reliable.

distribution of the bamboo fibers. The bamboo fiber is made up of layered cell walls where each cell is consisted of the crystal cellulose embedded in the amorphous matrix of the hemicellulose and lignin. The study on the structures and mechanical response of bamboo constituents associated with a future investigation of the interfacial interaction between the cellulose and the matrix of hemicellulose and lignin during the mechanical deformation can enable us to figure out the relationship between the microstructure and mechanical performance of bamboo fibers. Our work on the mechanical response of bamboo cell wall constituents can provide a fundamental understanding of the mechanical behavior of the bamboo cell wall in the fiber. As the bamboo fibers are the source of mechanical properties for bamboo, an underlying understanding of the mechanical behavior of bamboo fibers provides an insight into the macro-mechanical properties of bamboo. It indicates our work on the molecular conformation associated with the microstructural evolution for the bamboo constituents during the tensile deformation lays a foundation to figure out the macroscopic behavior of bamboo. In this work, it is found that the deformation of cellulose is mainly associated with the linearization and slippage of the polymer chains and the normal stress dominated fracture mechanism is the key to the failure of the hemicellulose whereas the shear stress dominated fracture mechanism is the main failure mode for the lignin. Such understanding on the relationship between the microstructure and mechanical properties of bamboo cell wall constituents can inspire us to fabricate a structural material with excellent mechanical properties. In order to improve the properties of processed bamboo, it is suggested the bamboo should be processed to minimize the cellulose microfibril angle, i.e. the angle between the cellulose microfibrils and the axial/longitudinal direction along the bamboo culm, so that the bamboo mechanical properties along the particular direction could be maximized. At the same time, the bamboo product could undergo the delignification process to reduce the lignin content in the structure so as to minimize the occurrence of a shear fracture induced by the lignin failure, which can also significantly improve the properties. Meanwhile, the performance of bamboo is deteriorated when exposed to the environment and the untreated bamboo just has a service life of only 2–5 years [67]. The bottom-up model of bamboo can also be applied to study the role of temperature and humidity in the performance of the bamboo contributing to figure out the origin of the deterioration of mechanical properties. The durability of bamboo can be improved by controlling the deteriorated factors. For example, we are inspired to remove the structure that has a negative effect on the mechanical properties and to synthesize the structure that has a positive influence on the properties.

4. Conclusion

Bamboo has better mechanical properties than timbers and its strength-to-weight ratio is greater than that of structural steel making it the next green reinforcement in the construction industry. However, its anisotropic properties across and along the culm hinder its use as the structural material. As the bamboo fibers made up of layered cell walls mainly provides the mechanical properties of bamboo, a study on the mechanical response of bamboo cell wall constituents is prerequisite to figure out the anisotropic mechanical properties. In our work, the stress-strain response during the tensile deformation at the strain of 10^8 s^{-1} of the cellulose, hemicellulose, and lignin is studied by the molecular dynamics simulations with the autonomous basin climbing algorithm. The molecular configurational changes at different strains are characterized and the relationship between the molecular conformation and the energy is examined. The results of this work can be summarized as follows:

(1) It is found that the non-bonded interaction and the slippage of the stretched polymer chains bonds play a dominant role in the high tensile stress of the crystal cellulose.
(2) The non-bonded interaction plays a significantly role at the beginning deformation stage of the modeled amorphous hemicellulose and lignin. As the deformation progresses, the change of the chain configurations such as the bond angle bending and the chain rotation is dominant associated with obvious variations of the angle related energy and the dihedral angle related energy. When the crack occurs, the stretched polymer chains near the cracked region move towards the aligned direction.
(3) As the hemicellulose is the branched polymer with short chains whereas the lignin is the crosslinked polymer with a network structure, the amorphous lignin has a higher stress than the amorphous hemicellulose. The normal stress dominated fracture mechanism is the key to the failure of the hemicellulose whereas the shear stress dominated fracture mechanism is the main failure mode for the lignin.

The thorough understanding on the mechanical response of bamboo constituents associated with a future investigation of the interfacial interaction between the cellulose and the matrix of the hemicellulose and lignin during the mechanical deformation can enable us to figure out the relationship between the microstructure and mechanical performance of bamboo fibers. As the source of mechanical properties for the bamboo, an underlying understanding on the mechanical behavior of bamboo fibers provides an insight into the macro-mechanical properties of bamboo. In this work, it is found that the breakage of the crystal cellulose is related to the polymer chains slippage at the (110) plane, which indicates that the crystal orientation of the cellulose microfibrils can be modified to ensure the strong interaction between the cellulose (110) plane and the matrix. Through the non-bonded interaction with the amorphous structure, the slippage of cellulose at the (110) plane can be resisted, which improves the cell wall mechanical properties. Through this example, it is learned that the fundamental understanding on the mechanical response of the cell wall constituents inspires us to engineer these constituents for higher mechanical properties. At the same time, the bamboo product could undergo the delignification process to reduce the lignin content in the structure, so as to minimize the occurrence of a shear fracture induced by the lignin failure, which can also significantly improve the properties. Furthermore, the bottom-up model of bamboo can also be applied to study the role of temperature and humidity on the performance of bamboo contributing to figure out the origin of the deterioration of mechanical properties. The durability of bamboo can be improved by controlling the deteriorated factors. For example, we are inspired to remove the structure that has a negative effect on the mechanical properties and to synthesize the structure that has a positive influence on the properties.

Acknowledgments

The authors are grateful to the support from the Research Grants Council (RGC) in Hong Kong through the General Research Fund (GRF) with the Grant No. 11255616.

References

[1] Sukmawan R, Takagi H, Nakagaito AN. Strength evaluation of cross-ply green composite laminates reinforced by bamboo fiber. Compos B Eng 2016;84:9–16.
[2] Shangguan WW, Gong YC, Zhao RJ, Ren HQ. Effects of heat treatment on the properties of bamboo scrimber. J Wood Sci 2016;62:383–91.
[3] Lima HC, Willrich FL, Barbosa NP, Rosa MA, Cunha BS. Durability analysis of bamboo as concrete reinforcement. Mater Struct 2007;41(5):981–9.
[4] Habibi MK, Tam L-H, Lau D, Lu Y. Viscoelastic damping behavior of structural bamboo material and its microstructural origins. Mech Mater 2016;97:184–98.
[5] Habibi MK, Lu Y. Crack propagation in bamboo's hierarchical cellular structure. Sci Rep 2014;4(5598):1–7.
[6] Dixon PG, Gibson LJ. The structure and mechanics of Moso bamboo material. J R Soc Interface 2014;11(99):1–12.
[7] Gibson LJ. The hierarchical structure and mechanics of plant materials. J R Soc Interface 2012;9(76):2749–66.

[8] Li HT, Zhang QS, Huang DS, Deeks AJ. Compressive performance of laminated bamboo. Compos B Eng 2013;54:319–28.
[9] Sharma B, Gatóo A, Bock M, Ramage M. Engineered bamboo for structural applications. Construct Build Mater 2015;81(15):66–73.
[10] Ogunwusi AA, Onwualu AP. Prospects of multi-functional utilisation of bamboo in Nigeria. Chem Mater Res 2013;2(8):58–61.
[11] Verma CS, Sharma NK, Chariar VM, Maheshwari S, Hada MK. Comparative study of mechanical properties of bamboo laminate and their laminates with woods and wood based composites. Compos B Eng 2014;60:523–30.
[12] Verma CS, Chariar VM. Development of layered laminate bamboo composite and their mechanical properties. Compos B Eng 2012;43(3):1063–9.
[13] Li HT, Su JW, Zhang QS, Deeks AJ, Hui D. Mechanical performance of laminated bamboo column under axial compression. Compos B Eng 2015;79:374–82.
[14] Reynolds T, Sharma B, Harries K, Ramage M. Dowelled structural connections in laminated bamboo and timber. Compos B Eng 2016;90:232–40.
[15] Wang F, Shao Z, Wu Y. Mode II interlaminar fracture properties of Moso bamboo. Compos B Eng 2013;44(1):242–7.
[16] Chung KF, Yu WK. Mechanical properties of structural bamboo for bamboo scaffoldings. Eng Struct 2002;24(4):429–42.
[17] Hebel DE, Javadian A, Heisel F, Schlesier K, Griebel D, Wielopolski M. Process-controlled optimization of the tensile strength of bamboo fiber composites for structural applications. Compos B Eng 2014;67:125–31.
[18] Choi BK, Yoon GH, Lee S. Molecular dynamics studies of CNT reinforced aluminum composites under uniaxial tensile loading. Compos B Eng 2016;91:119–25.
[19] Lau TT, Kushima A, Yip S. Atomistic simulation of creep in a nanocrystal. Phys Rev Lett 2010;104(17). 175501–1-5.
[20] Jian W, Tam L-H, Lau D. Atomistic study of interfacial creep behavior in epoxy-silica bilayer system. Compos B Eng 2018;132:229–36.
[21] Tam L-H, Zhou A, Yu Z, Qiu Q, Lau D. Understanding the effect of temperature on the interfacial behavior of CFRP-wood composite via molecular dynamics simulations. Compos B Eng 2017;109:227–37.
[22] Kim B, Choi J, Yang S, Yu S, Cho M. Multiscale modeling of interphase in cross-linked epoxy nanocomposites. Compos B Eng 2017;120:128–42.
[23] Ranganathan R, Ozisik R, Keblinski P. Viscoelastic damping in crystalline composites: a molecular dynamics study. Compos B Eng 2016;93:273–9.
[24] Koo B, Subramanian N, Chattopadhyay A. Molecular dynamics study of brittle fracture in epoxy-based thermoset polymer. Compos B Eng 2016;95:433–9.
[25] Yang H, Li F, Chan TW, Liu L, Zhang L. A simulation study on the effect of spring-shaped fillers on the viscoelasticity of rubber nanocomposite. Compos B Eng 2015;74:171–7.
[26] Yaphary YL, Yu Z, Lam RHW, Hui D, Lau D. Molecular dynamics simulations on adhesion of epoxy-silica interface in salt environment. Compos B Eng 2017;131:165–72.
[27] Nishiyama Y, Langan P, Chanzy H. Crystal structure and hydrogen-bonding system in cellulose Iβ from synchrotron X-ray and neutron fiber diffraction. J Am Chem Soc 2002;124(31):9074–82.
[28] Nishiyama Y. Structure and properties of the cellulose microfibril. J Wood Sci 2009;55(4):241–9.
[29] Ebringerová A, Hromádková Z, Heinze T. Hemicellulose. Springer Berlin Heidelberg; 2005.
[30] Scheller HV, Ulvskov P. Hemicelluloses. Plant Biol 2010;61(1):263–98.
[31] Vanholme R, Demedts B, Morreel K, Ralph J, Boerjan W. Lignin biosynthesis and structure. Plant Physiol (Wash D C) 2010;153(3):895–905.
[32] Youssefian S, Rahbar N. Molecular origin of strength and stiffness in bamboo fibrils. Sci Rep 2015;11116:1–13.
[33] Youssefian S, Jakes JE, Rahbar N. Variation of nanostructures, molecular interactions, and anisotropic elastic moduli of lignocellulosic cell walls with moisture. Sci Rep 2017;2054:1–9.
[34] Yan X, Cao P, Tao W, Sharma P, Park HS. Atomistic modeling at experimental strain rates and timescales. J Phys D Appl Phys 2016;49(493001):1–19.
[35] Laio A, Parrinello M. Escaping free-energy minima. Proc Natl Acad Sci USA 2002;99(20):12562–6.
[36] Shenogin S, Ozisik R. Simulation of plastic deformation in glassy polymers: atomistic and mesoscale approaches. J Polym Sci, Part B: Polym Phys 2005;43(8):994–1004.
[37] Cao P, Lin X, Park HS. Strain-rate and temperature dependence of yield stress of amorphous solids via a self-learning metabasin escape algorithm. J Mech Phys Solid 2014;8:239–50.
[38] Wegst UGK, Bai H, Saiz E, Tomsia AP, Ritchie RO. Bioinspired structural materials. Nat Mater 2015;14:23–36.
[39] Bello OS, Adegoke KA, Oyewole RO. Biomimetic materials in our world: a review. IOSR J Appl Chem 2013;5:22–35.
[40] Meyers MA, Chen PY, Lin AYM, Seki Y. Biological materials: structure and mechanical properties. Prog Mater Sci 2008;53:1–206.
[41] Accelrys Software Inc. Materials Studio. 2007.
[42] Fan Y, Yip S, Yildiz B. Autonomous basin climbing method with sampling of multiple transition pathways: application to anisotropic diffusion of point defects in hcp Zr. J Phys Condens Matter 2014;26(365402):1–16.
[43] Gomes TC, Skaf MS. Cellulose-builder: a toolkit for building crystalline structures of cellulose. J Comput Chem 2012;33(14):1338–46.
[44] Wen JL, Sun SL, Xue BL. Quantitative structural characterization of the lignins from the stem and pith of bamboo (Phyllostachys pubescens). Holzforschung 2013;67:613–27.
[45] Wu GL, Shah DU, Janecek ER, Burridge HC, Reynolds TPS, Fleming PH, Linden PF, Ramage MH, Scherman OA. Predicting the pore-filling ration in lumen-impregnated wood. Wood Sci Technol 2017;51:1277–90.
[46] Calonego FW, Severo TD, Cunha AR, Gaia DC. Use of glass transition temperature for stabilization of board's cracks of Eucalyputs grandis. An Acad Bras Cience 2010;82:791–7.
[47] Al-Ostaz A, Wu W, Cheng AHD, Song CR. A molecular dynamics and micro-poromechanics study on the mechanical properties of major constituents of hydrated cement. Compos B Eng 2010;41(7):543–9.
[48] Gou J, Liang Z, Zhang C, Wang B. Computational analysis of effect of single-walled carbon nanotube rope on molecular interaction and load transfer of nanocomposites. Compos B Eng 2005;36(6–7):524–33.
[49] Li Y, Wang S, Wang Q. Enhancement of tribological properties of polymer composites reinforced by functionalized graphene. Compos B Eng 2017;120:83–91.
[50] Christopher MB. Polarizable force fields for molecular dynamics simulations of biomolecules vol. 5. John Wiley & Sons Ltd; 2015. p. 241–54.
[51] Sun H. COMPASS: an ab Initio force-field optimized for condensed-phase applications-overview with details on alkane and benzene compounds. J Phys Chem B 1988;102:7338–64.
[52] Plimpton S. Fast parallel algorithms for short-range molecular dynamics. J Comput Phys 1995;117(1):1–19.
[53] Fan Y, Osetskiy YN, Yip S, Yidiz B. Mapping strain rate dependence of dislocation-defect of dislocation-defect interactions by atomistic simulations. Proc Natl Acad Sci Unit States Am 2013;11(44):17756–61.
[54] Lide Jr. DR. A survey of carbon-carbon bond lengths. Tetrahedron 1962;17(3–4):125–34.
[55] Tamagawa K, Kimura TM. Molecular structure of benzene. J Mol Struct 1976;30(2):243–53.
[56] Streitwieser Jr. A, Heathcock CH. Introduction to organic chemistry. Collier Macmillan Publishers; 1985.
[57] Cottrell TL. The strengths of chemical bonds. Butterworths Scientific Publications; 1954.
[58] Heiner AP, Sugiyama J, Teleman O. Crystalline cellulose Iα and Iβ studied by molecular dynamics simulation. Carbohydr Res 1995;273:207–23.
[59] Kroon-Batenburg LMJ, Kroon J. The crystal and molecular structures of cellulose I and II. Glycoconj J 1997;14:677–90.
[60] Pethrick RA, Amornsakchai T, North AM. Introduction to molecular motion in polymers. Whittles Publishing; 2011.
[61] Hossain D, Tschopp MA, Ward DK, Bouvard JL, Wang P, Horstemeyer MF. Molecular dynamics simulations of deformation mechanisms of amorphous polyethylene. Polymer 2010;51(25):6071–83.
[62] Grandbois M, Beyer M, Rief M, Clausen-Schaumann H, Gaub HE. How strong is a covalent bond? Sciences 1999;283:1727–30.
[63] Martin KB, Hauke CS. Mechanochemistry: the mechanical activation of covalent bonds. Chem Rev 2005;105:2921–48.
[64] Aklonis JJ. Mechanical properties of polymers. J Chem Education 1981;58:892–7.
[65] Loo LS, Cohen RE. Gleason KK,Chain. Mobility in the amorphous region of nylon 6 observed under active uniaxial deformation. Sciences 2000;288:116–9.
[66] Zhao JH, Yu PS, Dong SH. The influence of crosslink density on the failure behavior in amorphous polymers by molecular dynamics simulations. Materials 2016;9:234–44.
[67] Sulaeman A, Dungani R, Nurudin N, Hartati S, Karliati T, Aditiawati P, Hadiyane A, Suhaya Y. Sulistyono, Review on quality enhancement of bamboo utilization: preservation, modification and applications. Asian J Plant Sci 2018;17:1–18.